Journal of Ceramic Processing Research. Vol. 19, No. 2, pp. 154~170 (2018)

J O U R N A L O F
Ceramic Processing Research

Effect of strontium on the structural and piezoelectric properties of the sol gel processed barium titanate

Abdelhak El Ghandouri[a], Salaheddine Sayouri[a,*], TajEddine Lamcharfi[b] and Lahoucine Hajji[c]

[a]*LPTA, Department of physics, FSDM B.P. 1796, Fez. Morocco*
[b]*LSSC, FST Street Immouzar, B.P. 2202 Fez, Morocco*
[c]*LMCN, F.S.T.G University Cadi Ayyad Marrakech, Morocco*

Structural, dielectric and piezoelectric properties of nanopowders of pure and strontium-doped $BaTiO_3$ ($Ba_{1-x}Sr_x)TiO_3$ (x = 0.00; 0.10; 0.20; 0.30 and 0.40), synthesized by the sol gel process, have been investigated. The samples crystallize in the pure perovskite structure and transform from tetragonal to pseudocubic under doping with Sr. The calculated average crystallite size was about 30 nm. Dielectric parameters (dielectric permittivity and losses) were determined. Sr doping gives rise to a decrease of the ferro-to-paraelctric transition temperature and to an enhancement of the Positive Temperature Coefficient of Resistivity (PTCR). Piezoelectric parameters were also determined and their thermal behavior investigated.

Key words: (Ba, Sr)TiO_3 ceramics, Sol Gel, Dielectric properties, Complex impedance, PTCR and Piezoelectric properties.

Introduction

Barium Titanate ($BaTiO_3$) is a perovskite type material, which is known for its various properties: high dielectric constant, ferroelectric behavior below 130 °C, spontaneous polarization and non-linear optical coefficients. The origin of ferroelectricity in $BaTiO_3$ derives from the displacement of ions relative to each other. It is well known that dielectric properties of $BaTiO_3$ can be systematically modified by chemical substitution of barium and/or titanium by a wide variety of isovalent and aliovalent dopants. The study of this lead-free compound is interesting not only for basic research but also for its applications in many industrial sectors, such as Multilayer Ceramic (MLCCs), non-volatile ferroelectric FRAM's memories, detection of gaseous pollutants like CO, Positive temperature coefficient resistors (PTCR), optical data storage at High density, ultrasonic transducer [1-5].

Strontium-doped barium titanate (BST) has been widely used for various applications, particularly in the fields of electronics and telecommunications, because of its high dielectric constant, large electric field tunabilities, relatively low dielectric losses, variable Curie temperature depending on Sr content, large polarization and large induced strains [6-9].

The aim of the present work is the synthesis, by the sol gel process, and characterization of pure and strontium doped $BaTiO_3$ materials, in view of investigation of the influence of Sr-doping on their structural microstructural and dielectric properties. It is known that synthesis of $BaTiO_3$ by conventional methods needs high calcination temperatures [10]. In this regard, Our interest consists also in optimizing this parameter.

To this end, we have prepared a series of sol gel processed Sr-doped BT, which chemical formula is $Ba_{1-x}Sr_xTi_{1+x/4}O_3$, through the destabilization of colloidal solution (DCS) method, and their structure and dielectric properties were investigated.

*Corresponding author:
Tel : +(212)673785288
Fax: +212-5-35-73-33-49
E-mail: ssayouri@gmail.com

Experimental Procedure

Samples preparation

Strontium-doped barium titanate powders, ($Ba_{1-x}Sr_x)TiO_3$ (BST_x), were prepared by the sol-gel route using titanium isopropropoxide: $Ti[OCH(CH_3)_2]_4$ (purity ≥ 97%), Barium acetate $C_4H_6Ba\ O_4$ (99%), strontium acetate $C_4H_6SrO_4$ as precursors, in adequate proportions.

Distilled water, acetic acid CH_3COOH and ethanol C_2H_5OH as solvent.

The following flow chart details the experimental procedure of preparation of the samples (Fig. 1).

Characterisation equipment

Crystal structures of $Ba_{1-x}Sr_xTiO_3$ powders were determined by X-ray diffraction (Diffractometer system= XPERT-PRO) using a CuKα radiation (λ = 1.54059 Å), FTIR spectra (VERTEX 70) and Raman spectra (SENTERRA). Microstructure of powders and ceramics was characterized using a scanning electron microscope (SEM) (Quanta 200 FEI). For dielectric measurements, the powders were compressed into discs of about

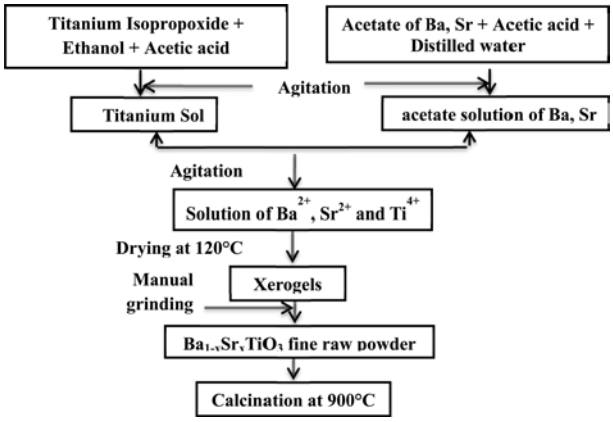

Fig. 1. Flow chart of the preparation of BST_x samples.

12 mm as diameter and sintered at 1200 °C for 6 hrs.

The dielectric properties were measured by an impedance analyzer (HP 4284A), in the temperature and frequency ranges [ambiente, 500 °C] and [20 Hz, 1 MHz], respectively.

Results and Discussion

Structural characterizations

Fig. 2(a) shows XRD patterns of the BT powders calcined at 800 °C and 900 °C, revealing that the formation of the pure $BaTiO_3$ phase is complete at 900 °C. Zoom in on the peak (110) shows a shifting of this peak to lower angles, and hence an improvement in powder crystallinity by increasing the calcination temperature from 800 °C to 900 °C (Fig. 2(b)).

Table 1 shows FWHM to decrease with increasing temperature indicating an increase in the crystallite size.

Fig. 3 shows XRD diffrctogramms of $Ba_{1-x}Sr_xTiO_3$ (x = 0.00; 0.10; 0.20; 0.30 and 0.40) powders calcined at 900 °C during 3h, showing that all samples crystallize in the pure perovskite phase, but however with the presence of few traces of impurities. This result is consistent with several other studies [11-13].

Furthermore, since the strontium doping rate was increased, the diffraction peaks slightly shift toward higher angles, as shown in fig. 3(b); indeed, zoom in on the peak (111) in the range $38° < 2\theta < 40°$ shows clearly that Sr-doping moves the position of this peak towards highest angles. The $BaTiO_3$ lattice is contracted by incorporation of Sr atoms as the ionic radii of Ba^{2+} and Sr^{2+} are 1.49 and 1.32 Å, respectively, and then a lattice distortion would be induced. Sr-doping gives rise to a slight transformation from quadratic (pure BT) to pseudo-cubic phase (BSTx, x > 0.20) as revealed by the zoom in on the peak (200) in the range $44° < 2\theta < 47°$, showing that this large and asymmetric peak indicates the existence of two complementary peaks is clearly, observed around $2\theta = 45°09'$ and $2\theta = 45°36'$ in the pure sample (x = 0), and these two peaks tend to merge as observed for the three other compositions (Fig. 3c) while maintaining relatively large FWHM. Stabilization of the pseudocubic has also been reported [14].

The average crystallite size (ACS) of the $Ba_{1-x}Sr_xTiO_3$ samples was calculated using the Scherrer formula:

$$D = \frac{k * \lambda}{FWHM \ * cos\ \theta} \quad (1)$$

Where K = 0.9 is a constant, λ = 0.154059 nm is the wavelength of the source used and FWHM is the half-height width [15].

Table 2 shows the estimated average crystallite size of the as-prepared $Ba_{1-x}Sr_xTiO_3$ powders calcined at 900 °C for 3 h, assuming spherical shaped particles. It is observed that the ACS first decreases (x = 0.10) and then increases (x = 0.20, 0.30 and 0.40).

Fig. 4 and Table 2 show that as the strontium content

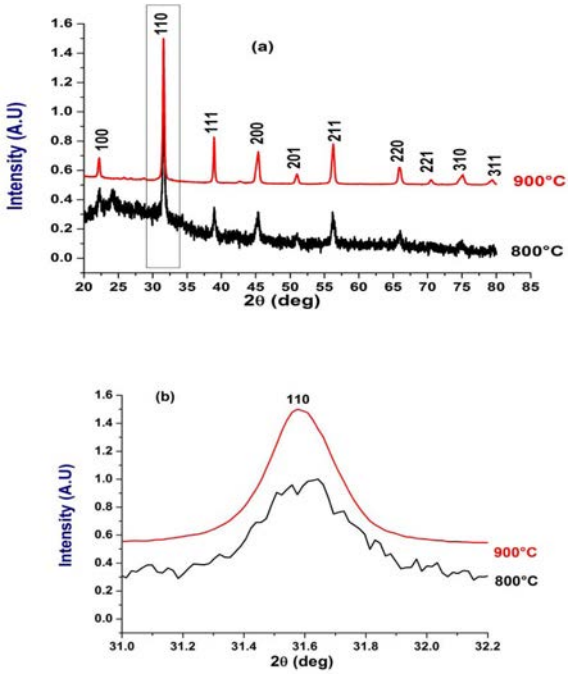

Fig. 2. (a) XRD pattern of BT powders calcined at 800 and 900°C, (b) zoom in on the peak (110).

Table 1. Structural parameters of BT powders calcined at different temperatures.

Calcination temperature	2θ	hkl	FWHM	Crystallite size (nm)	d-spacing (°A)
800 °C	31.6055	110	0.2342	35.25	2.8309
900 °C	31.5541	110	0.2175	37.95	2.8331

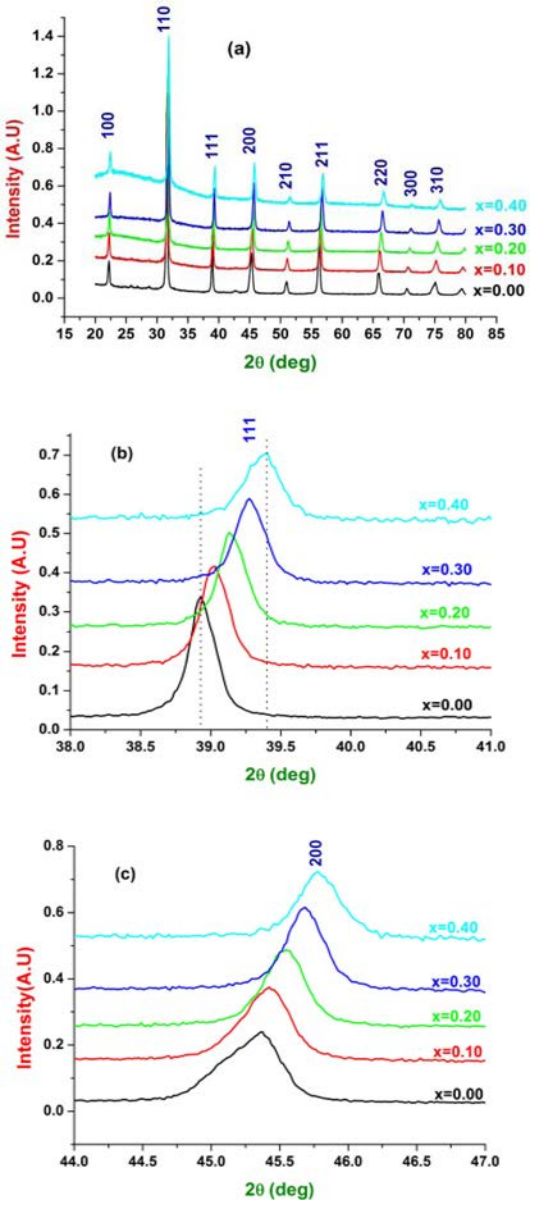

Fig. 3. (a) XRD pattern of $Ba_{1-x}Sr_xTiO_3$ powders calcined at 900 °C for 3 h, (b) zoom in on (111) peak and (c) zoom in on (200) peak.

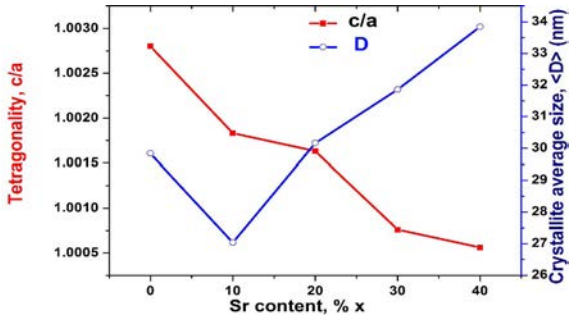

Fig. 4. Variation of tetragonality (c/a) and average crystallite size, <D> vs. x of $Ba_{1-x}Sr_xTiO_3$ powders calcined at 900 °C for 3 h.

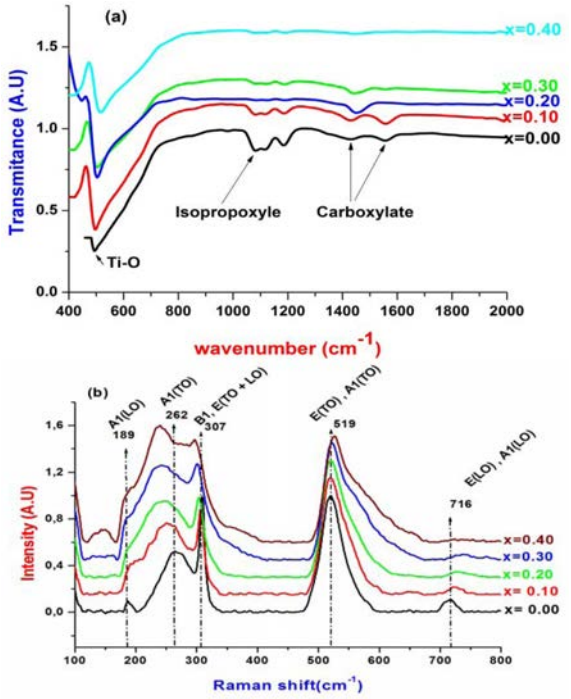

Fig. 5. (a) FTIR Spectra,(b) Raman spectra of $Ba_{1-x}Sr_xTiO_3$ calcined at 900 °C for 3 h

increases, the tetragonality of the structure decreases, and that for x > 0.20 in Sr, the structure stabilizes in the pseudo cubic one, due to electrostatic repulsions between 3d electrons of Ti^{4+} ions and 2p electrons of O^{2-} ions [16]. On the other hand, the elementary cell volume is reduced with Sr doping as seen in Table 2, probably due to the smaller ionic radius of Sr^{2+} (1.32 Å) compared to that of Ba^{2+} (1.49 Å).

Fig. 5(a) shows the FTIR spectra of the $Ba_{1-x}Sr_xTiO_3$ powders for different concentrations in Sr. The absorption band in the low frequency range from 400 cm^{-1} to 800 cm^{-1}, derived from the vibrations (vibrations of the

Table 2. Variation of lattice parameters, tetragolality, volume and crystallite size of $Ba_{1-x}Sr_xTiO_3$ powders calcined at 900 °C for 3 h.

$(Ba_{1-x}Sr_x)TiO_3$	Lattice parameters			Tetragonality	Structure	Volume $(Å)^3$	Average crystallite size (nm)
X	a (Å)	b (Å)	c (Å)	(c/a)			
0.00	4.0023	4.0023	4.0135	1.0028	Tetragonal	64.29	29.8401
0.10	3.9952	3.9952	4.0025	1.0018	Tetragonal	63.89	27.0336
0.20	3.9831	3.9831	3.9896	1.0016	Tetragonal	63.30	30.1661
0.30	3.9715	3.9715	3.9745	1.0007	Pseudo Cubic	62.69	31.8600
0.40	3.9638	3.9638	3.9660	1.0005	Pseudo Cubic	62.31	33.8436

TiO_6 octahedron) of the Ti-O isopropoxide groups [17]. Two intense bands at 1430 and 1556 cm^{-1} are assigned to symmetrical and antisymmetric vibrations respectively (stretching of barium and / or titanium-bound carboxylic groups (COO^-)) [18, 19]. Two bands lying between 1000 and 1200 cm^{-1} can be attributed to isopropyl groups bound to the titanium atoms in a monodentate mode and traces of the carbonate in small amount. The vibration band of the organic (carboxylic) groups, located in the frequency range between 900 and 1700 cm^{-1}, decreased with the increase of the strontium doping rate (it disappeared for x = 0.40, in conformity with XRD results), while the Ti-O absorption peaks become more prominent.

Fig. 5(b) shows the Raman spectra of the $Ba_{1-x}Sr_xTiO_3$ nano-powders obtained for different Sr content. The active Raman modes for $BaTiO_3$ characterizing the quadratic phase are displayed. The sharp bands around 189 cm^{-1} A1 (LO) and 307 cm^{-1} [B1, E (TO + LO)] and the wide bands around 262 cm^{-1} [A1 (TO), E (TO)] and 716 cm^{-1} [A1 (LO), E (LO)] are characteristic peaks of the quadratic phase of $BaTiO_3$ [20, 21].

It is observed on these Raman spectra that as x increases (x > 0), intensities of the peaks mentioned above decrease with a slight frequency range shift, pointing out the effect of Sr on the BT structure. In particular, the peak intensity of the band located at 716 cm^{-1} characteristic of the quadratic phase, undergoes a strong decrease (x > 0.20), indicating the transition from quadratic to pseudo cubic phase.

Observations made on Raman spectra are in good agreement of those of revealed by XRD analysis.

SEM characterization

Figs. 6 (a) and (b) show the SEM micrographs of $Ba_{1-x}Sr_xTiO_3$ (x = 0.20 and 0.30) samples sintered at 1200 °C for 6h. These images show well-developed grain morphology and a dense microstructure. The mean grain size, estimated for the whole range of x,

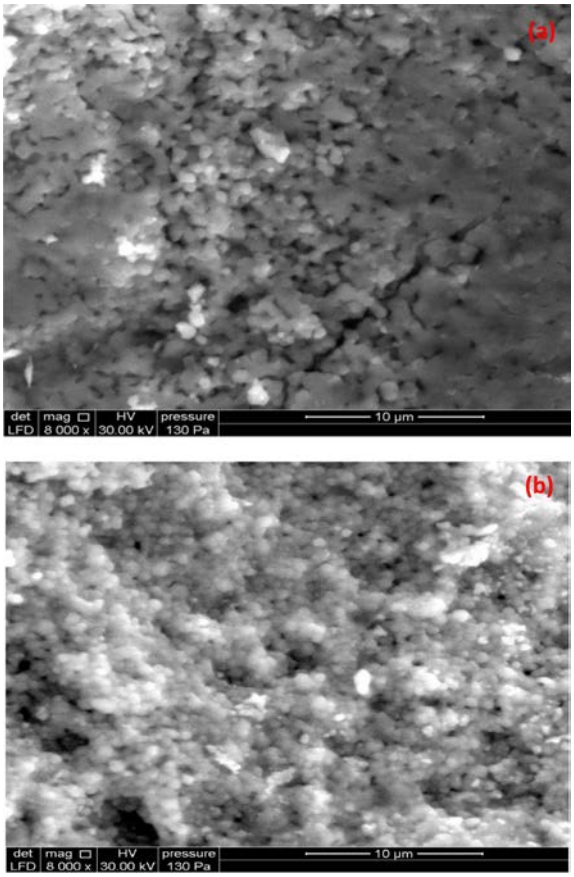

Fig. 6. Scanning Electron Micrographs (SEM) for $BS_{20}T$ (a) and $BS_{30}T$ (b).

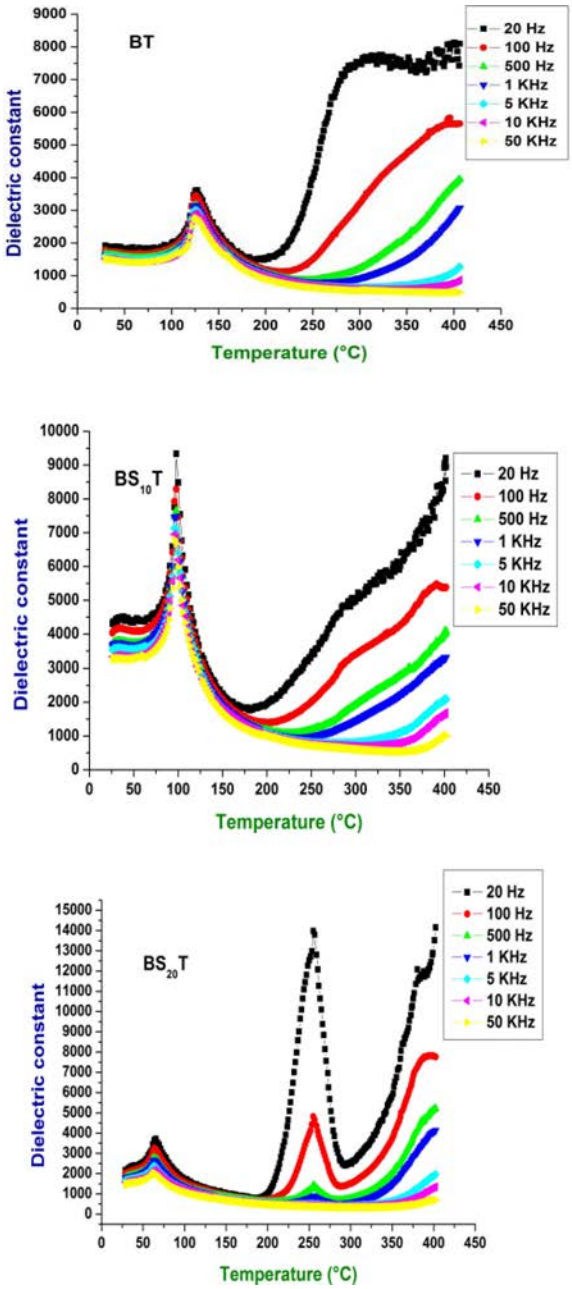

Fig. 7a. Variation of the real part of permittivity (ε_r) with temperature at different frequencies (20 Hz-50 KHz) for the $Ba_{1-x}Sr_xTiO_3$ sintered at 1200 °C for 6 h.

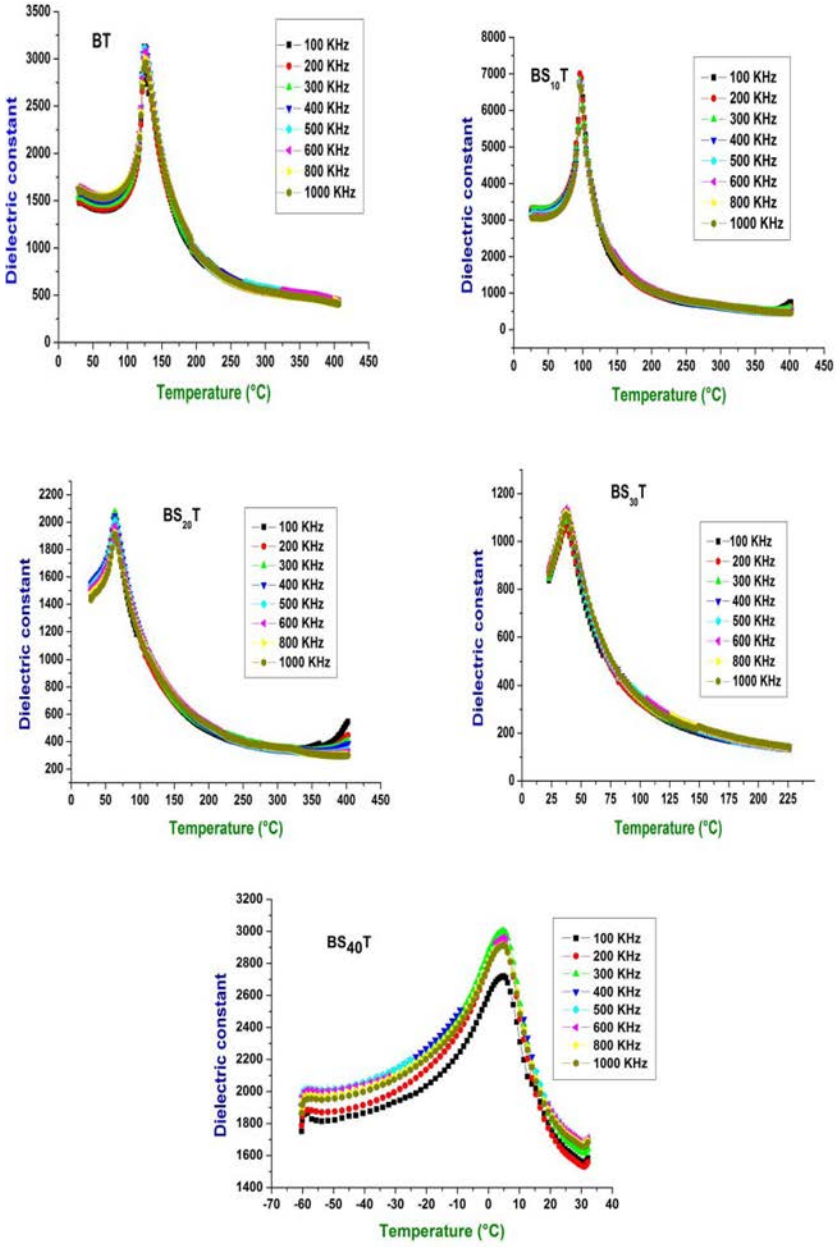

Fig. 7b. Variation of the real part of permittivity (ε_r) with temperature at different frequencies (100 kHz-1000 kHz) for the $Ba_{1-x}Sr_xTiO_3$ sintered at 1200 °C for 6 h.

varies between 3.6 μm (x = 0.00) to 830 nm (x = 0.40). This result may be associated with the substitution of the larger Ba^{2+} ion by the smaller Sr^{2+} ion, structural defects, or the formation of agglomerates.

Dielectric studies

Curie temperature and phase transitions

$BaTiO_3$ is known as a typical ferroelectric material with three phase transitions: tetragonal-cubic at about 125 °C, orthorhombic-tetragonal around 5 °C and orthorhombic-rhombohedral at approximately −90 °C [22].

In order to investigate the dielectric properties of the BST samples, the latter were prepared under the form of discs with a diameter of about 10 mm and a thickness of about 1.2 mm, followed by a sintering process at 1200 °C for 6 hours.

The dielectric properties were studied as functions of temperature and for different frequencies (20 Hz-1MHz). Figs. 7 and 8 show the thermal behavior, for different frequencies, of the real part of the permittivity, ε'_r, and dielectric losses for $Ba_{1-x}Sr_xTiO_3$ (x = 0.00; 0.10; 0.20; 0.30 and 0.40. Sharp peaks (maximum of ε'_r (T)) are observed for x = 0 and 0.10 at the temperatures T_c = 125.3 °C and 95.7 °C, respectively, corresponding to the ferro-to-paraelectric phase transition (Fig. 7a). This maximum becomes more diffuse (x > 0.10) and shifts to lower values of temperature with increasing x

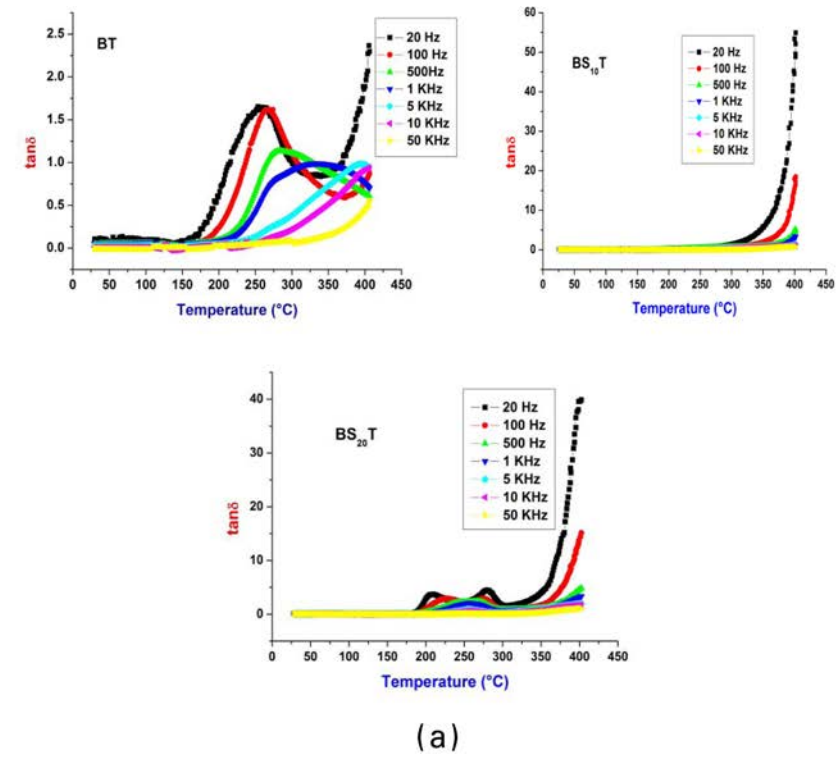

(a)

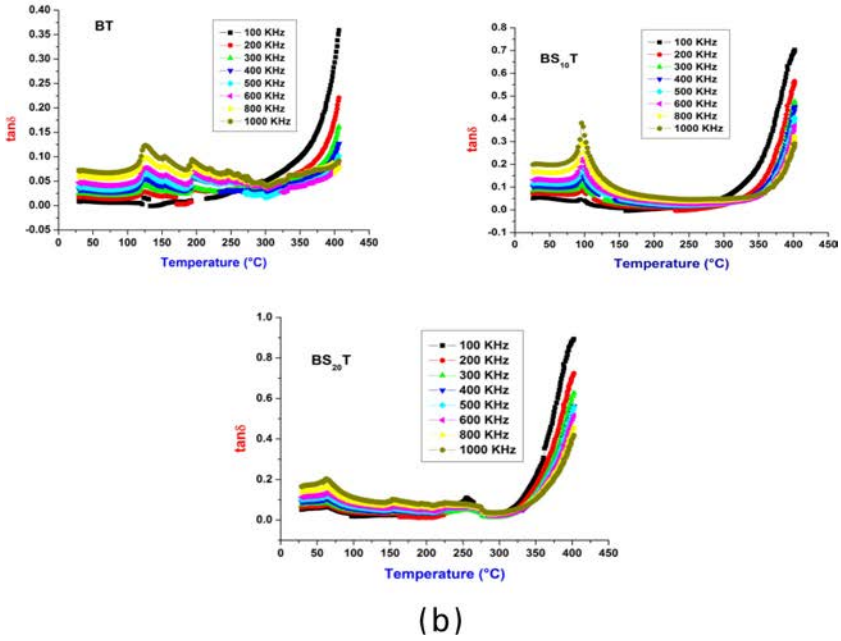

(b)

Fig. 8a. Variation of dielectric loss (tan δ) with temperature at different frequencies (20 Hz-50 KHz) for $Ba_{1-x}Sr_xTiO_3$ sintered at 1200 °C for 6 h.

Fig. 8b. Variation of dielectric losses (tan δ) with temperature at different frequencies (100 KHz-1000 KHz) for $Ba_{1-x}Sr_xTiO_3$ sintered at 1200 °C for 6 h.

(Figs. 7a and 7b). At the ferro-to-paraelectric transition (driven by temperature), the BST materials undergoe a symmetry change from tetragonal to cubic, and this'high-temperature' phase is almost always more disordered, i.e., has a higher symmetry than the 'low-temperature' phase. Our studied compositions of Sr doped $BaTiO_3$ (disorder is introduced by Sr ions) show tetragonal (undoped sample) or pseudo-cubic structures, as confirmed by XRD and Raman studies, and the observed ferro-to-paraelectric phase transitions are consistent with the structural studies.

We also observe that (ε'_r)max (maximum of the permittivity at the transition temperature) decreases with increasing frequency in the considered interval, from 20

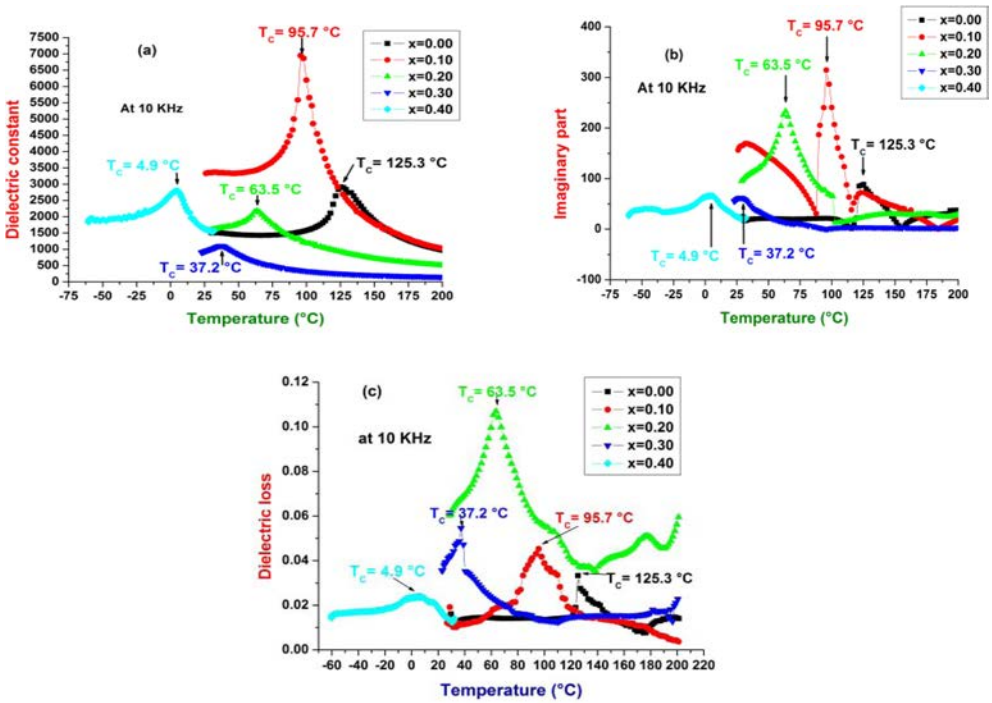

Fig. 9. Thermal variations of the real part ε'_r (a), the imaginary part ε'' (b) of the permittivity and the dielectric loss (c) of the $Ba_{1-x}Sr_xTiO_3$ at 10 kHz.

to 50 kHz (Fig. 7a) and from 100 to 1000 kHz (Figs. 7), and that for $x > 0.10$ this decrease is accompanied with relaxation (Figs. 7) [23]. Moreover, an anomaly is observed above the transition temperature in the permittivity curves of the samples with $x = 0.00$, 0.10, 0.20 (Fig. 7a), which may due to an extrinsic phenomenon [24].

Thermal behavior of dielectric losses (tan δ) is given in Figs. 8a and 8b. Low values of this parameter were recorded, with the appearance of a maximum around

Table 3. Some $Ba_{1-x}Sr_xTiO_3$ dielectric parameters compared with other studies.

Method of preparation	Ceramics	T_f (Sintering)(°C)	T_c(°C)	ε_r	tanδ	Reference
Pechini	$BaTiO_3$	1350 (3h)	125	7000(105 kHz)	0.025	Adelina.I et al[25]
Sol-gel		1300	112	3250(100kHz)	0.034	W.Li et al[29]
Sol-gel		1200(6h)	125.3	2915(10 kHz)	0.029	Present work
Sol-gel	$Ba_{0.9}Sr_{0.1}TiO_3$	1350(6h)	102	10800(100kHz)	0.038	Manoj.K et al[26]
Sol-gel		1400(4h)	109	5694(1kHz)	0.043	A.Lanculescu et al[28]
Sol-gel		1300	93	4160(100kHz)	0.032	W.Li et al[29]
Sol-gel		1200(6h)	95.7	6947(10 kHz)	0.045	Present work
Pechini	$Ba_{0.8}Sr_{0.2}TiO_3$	1350 (3h)	64	5100(105kHz)	0.06	Adelina.I et al[25]
Sol-gel		1400(4h)	78	5638(1kHz)	0.039	A.Lanculescu et al[28]
Sol-gel		1300	64	4000(100kHz)	0.026	W.Li et al[29]
Sol-gel		1200(6h)	63.5	2182(10 kHz)	0.106	Present work
sol–gel	$Ba_{0.7}Sr_{0.3}TiO_3$	1250	(amb)	1564(1 kHz)	0.58	Chanyaphak.Tet al [27]
Pechini		1350 (3h)	25	4000	0.0075	Adelina.I et al[25]
Sol-gel		1400(4h)	41	5482(1kHz)	0.038	A.Lanculescu et al[28]
Sol-gel		1300(2h)	40	3000(100kHz)	0.0275	
Sol-gel		1200(6h)	37.2	1055(10 kHz)	0.057	W.Li et al[29]
						Present work
Voie solide	$Ba_{0.6}Sr_{0.4}TiO_3$	1210(3h)	5	1500(1kHz)	0.026	L. Nedelcu et al [30]
Sol-gel		1200(6h)	4.9	2792(10 kHz)	0.0236	Present work

T_c. The strong increase of tan δ above T_c is consistent with the conductive character of the samples in the paraelectric phase. Table 3 gathers values of the dielectric parameters T_c, ε'_r max and tan δ for $Ba_{1-x}Sr_xTiO_3$ ceramics, together with some of those of the literature.

Fig. 9 illustrates thermal variations of the dielectric parameters ε'_r, ε" and tgδ, of the sample $BS_{0.20}T$, at the frequency 10 kHz. These variations are consistent with literature [31]. Moreover, as the transition temperature decreases with increasing x values, it is possible to obtain a ferroelectric material at a temperature near ambient temperature for a specific Sr concentration (in our case $0.3 < x < 0.4$).

Fig. 10 displays, as illustration, the frequency dependence of the permittivity, ε_r, at different temperatures for BT and $BS_{40}T$ samples; in the temperature range considered, ε_r shows a gradual decrease with rise in frequency. This decrease is due to the space charges, leading to the high permittivity and frequency dispersion, and indicating a thermally activated nature of the observed dielectric relaxation.

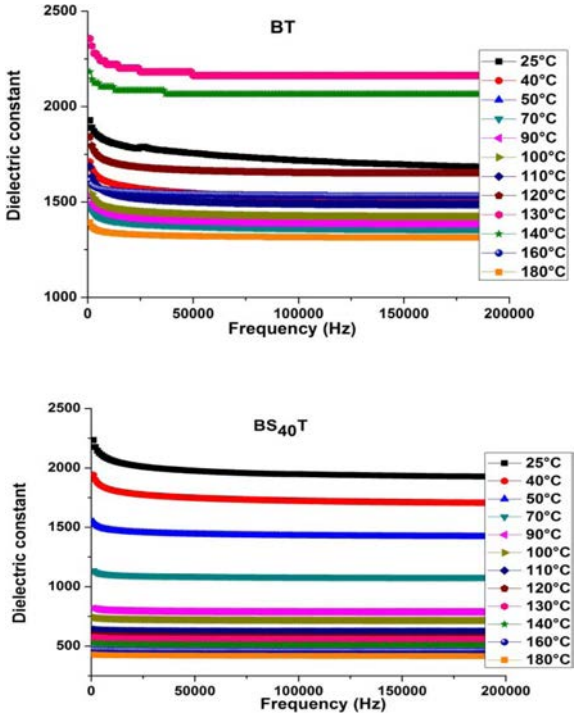

Fig. 10. Frequency dependence of permittivity of BT and $BS_{40}T$.

The ferroelectric-paraelectric phase transition and the Curie-Weiss law

Fig. 11 depicts the thermal variation of the inverse of the permittivity ($1 / \varepsilon'_r$). It is known that for a normal ferroelectric the ferro-to-paraelectric phase transition is of first order when $T_0 < T_C$ and a second order when $T_C = T_0$, where T_0 is the Curie-Weiss temperature defined by the following relation [32].

$$\frac{1}{\varepsilon_r} = \frac{T - T_C}{C} \tag{2}$$

The phase transition, which is of the first order for $Ba_{1-x}Sr_xTiO_3$ such that $x = 0.00$ and $x = 0.10$, transforms into the second order for the composition $x = 0.40$ (Fig. 11) [33].

Curie Weiss law is no longer valid in the case where relaxation and diffusness are present. Modified Uchino's law is the appropriate approach to fit the permittivity behavior above the temperature of the ferro-to-paraelectric phase transition. [34] expressed as follows:

$$\frac{1}{\varepsilon_r} = \frac{1}{\varepsilon_{r\,max}}\left[1 + \frac{(T - T_m)^{\gamma}}{2 * \delta^{\gamma}}\right] \tag{3}$$

Eq. 3 may be written under the following linear form:

$$\ln\left[\left(\left(\frac{\varepsilon_{r\,\max}}{\varepsilon_r}\right) - 1\right) * 2\right] = \gamma \ln(T - T_m) - \gamma \ln \delta \tag{4}$$

Where:

γ is an empirical coefficient that describes the diffuse nature of the transition.

$\gamma = 1$ for a conventional transition.

$1 < \gamma < 2$ for a diffuse transition.

$\gamma = 2$ for a relaxing ferroelectric, or totally diffuse.

δ indicates the degree of diffuseness of the peak

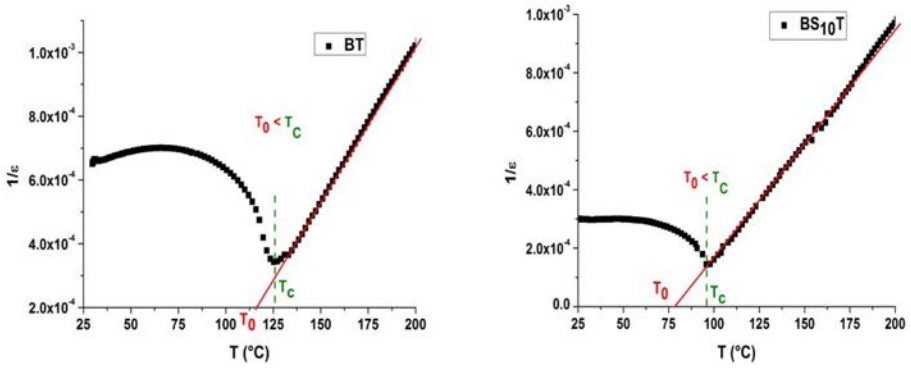

Fig. 11. Variation of 1/ε with temperature of the ceramics BT and $BS_{10}T$ at 10 kHz.

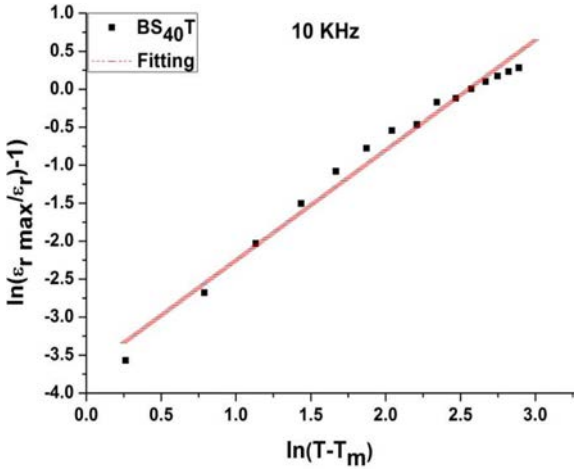

Fig. 12. Variation of $\ln(1/\varepsilon_r - 1/\varepsilon_{r\,max})$ as a function of $\ln (T-T_m)$ for $BS_{40}T$ ceramic.

Table 4. gathers γ values for BST_x samples.

Frequency (kHz)	$BS_{30}T$	$BS_{40}T$
1	1.1616	1.4895
10	1.1662	1.5550
50	1.1702	1.5092
100	1.1721	1.4177
200	1.1761	1.4583
400	1.1741	1.4576
600	1.1756	1.4512
800	1.1814	1.4403
1000	1.1834	1.4609

Fig. 12 illustrates the fit of the data to Eq. 4.

Fig. 12 shows a linear relationship between $\ln(T-T_m)$ and $\ln(1/\varepsilon_r - 1/\varepsilon_{r\,max})$ for the BS_xT samples at 10 kHz, with x = 0.40.

The increase of the γ factor (Table 4) shows that the phase transition becomes more diffuse with the increase of Sr content.

This diffuse phase transition can be influenced by factors such as disorder through local deformation and the fluctuation of microscopic composition [35]. The local strain may appear due to the ionic radius size of the site A (Ba^{2+} et Sr^{2+}) and the ions of site B (Ti^{4+}) of the perovskite structure ABO_3, which causes distortion of the TiO_6 octahedron giving rise to electric fields and local deformations. Therefore, the value of γ depends on the crystal structure, and thus the defects in the ceramic.

Complex impedance studies

In the perovskite system the main mode of charge transport is a multiple jump process. This jumping process occurs especially through the potential barriers that occur within the structure and the local atoms / ions environment.

In order to better understand the nature of conduction, we studied the complex impedance spectra of BS_xT samples. Figs. 13(a) and (b) show the impedance spectra ($Z'' = f(Z')$) of $BS_{10}T$ and $BS_{20}T$ samples, sintered at 1200 °C for 6h, measured at different temperatures, from 335 to 400 °C. For each temperature, the corresponding curves appear under the form of two depressed semicircles, suggesting the presence of both bulk and grain boundary effects in the studied samples. The high-frequency arc is related to the grain and the low-frequency arc to the grain boundary contribution. Impedance data from room temperature up to about 300 °C are not illustrated in Fig. 13 as they just showed a straight line with large slopes underlying the insulating character of the samples. It is observed on Fig. 13 that the slope of the lines decreases with increasing temperature, and hence they bend towards Z' axis, and that the corresponding radius of curvature decreases with increasing temperature, due to the increase of the conductivity of the samples.

The experimental data were adjusted using the Zview analysis software (version 3.1C), and the results are shown in Fig. 14, which are in good agreement with the experimental ones (Fig. 13). Moreover, each semicircle may be represented by an RC circuit, corresponding to individual component of the samples and providing a real representation of their electrical properties.

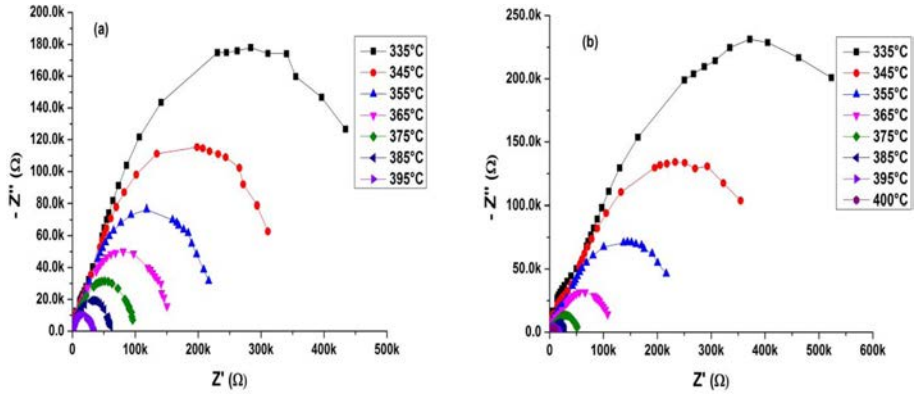

Fig. 13. Impedance curves corresponding to $BS_{10}T$ (a) and $BS_{20}T$ (b).

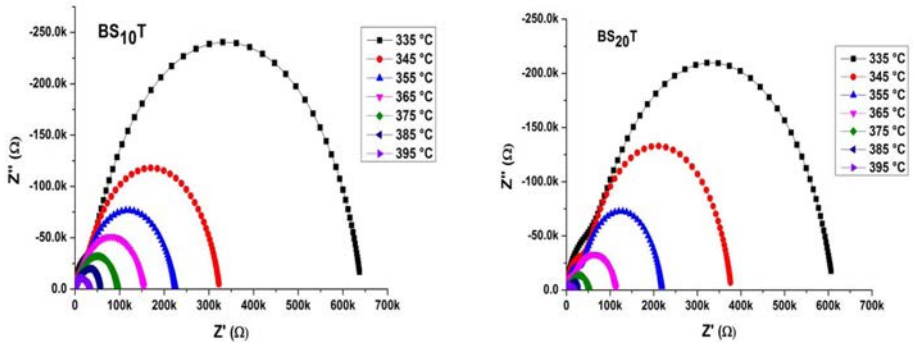

Fig. 14. Z '' as a function of Z ' for the ceramics $Ba_{1-x}Sr_xTiO_3$.

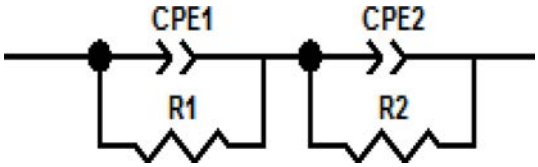

Fig. 15. Equivalent circuit of the $Ba_{1-x}Sr_xTiO_3$ceramic.

Results from impedance spectra have been approached by an equivalent circuit composed of two parallel elements (R, Q) connected in series, as shown in Fig. 15. R and Q represent the resistance and the constant phase element (CPE), respectively. Indeed, the fitting results show that the measured BS_xT capacitance response throughout the frequency range is not ideal, i.e., the BS_xT do not behave as pure capacitors, which may be due to the distribution of various relaxation times [36].

Hence, the effect of the grains (bulk) and the grain boundaries are represented by the parallel combinations R1-CPE1 and R2-CPE2, respectively.

Values of these parameters have been obtained from impedance data (Table 5). The equivalent capacitance, C, of a constant phase element and the relaxation frequency f_{relax} corresponding to a specific (R,Q) element can be calculated according to the following equations [37]:

$$C = (R^{1-n}Q)^{\frac{1}{n}} \quad (4)$$

$$f_{relax} = \frac{(RQ)^{-1/n}}{2\pi} \quad (5)$$

R: resistance (Ω)

Q: capacitance (F)

The value of the depression angle θ (in radians) is calculated from the following equation [38]:

$$n = 1 - \frac{2\theta}{\pi} \quad (6)$$

Where n is the arc depression factor. The values n = 1 and n = 0 represent an ideal capacitor and an ideal resistance, respectively.

Table 5 gathers the obtained fitting parameters.

The frequency dependence of Z' at different temperatures is shown in Fig. 16(a). It is observed that Z' decreases with increasing frequency and temperature, indicating the increase in ac conduction (σ_{ac}) in the samples. This increase in conduction may be explained as due to the contribution of defects such as oxygen deficiencies, and hence at high temperature, the contribution due to the latter is more dominant. At low frequencies, a significant decrease of Z' with increasing Sr content is observed. At high frequency, the value of Z' appears to be frequency independent for all temperatures, indicating that there is an increase in the concentration of defects with the rise of temperature leading to an increase of conductivity of the samples [39, 40]. The merging of the Z' curves in the higher frequency region is probably due to the release of space charges due to the reduction of the barrier properties of the samples. It is also observed that the frequency for which the curves, Z', coincide increases with the increase of the strontium content: 300 Hz for the pure BT and 40 kHz and 94 kHz for $BS_{10}T$ and $BS_{20}T$, respectively.

The variation of the imaginary part of the impedance (Z'') with the frequency at different temperatures is shown in Fig. 16(b). It is observed that Z'' increases with frequency, passes through a maximum that shifts towards higher frequencies on increasing both temperature and Sr content, and then decreases and tends to an almost constant value.

The width of the maximum may suggest the existence of a distribution of relaxation times [41] that can be calculated from the values of the angular frequencies corresponding to these maxima with the help of the following relation:

$$\tau = 1/\omega_{max} \quad (8)$$

Fig. 17 shows the variation of the relaxation time as a function of 1000/T. Values of the obtained activation energies are gathered in Table 6.

Conductivity studies.

In order to better understand the transport mechanism in the BST ceramics, the thermal electrical conductivity behavior was investigated. The conduction in a material

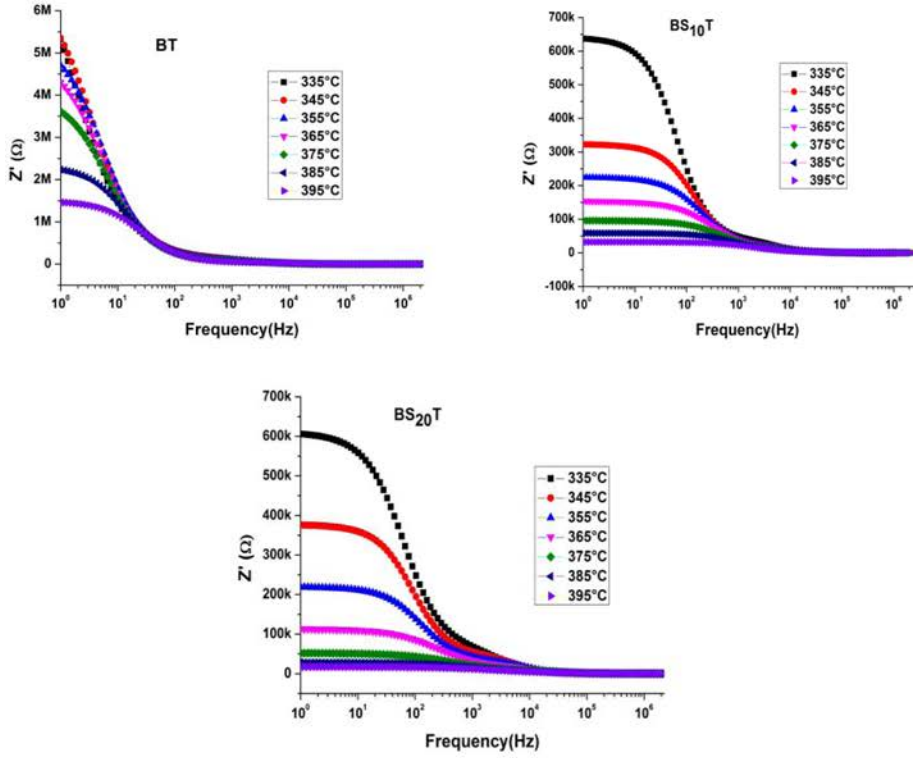

(a)

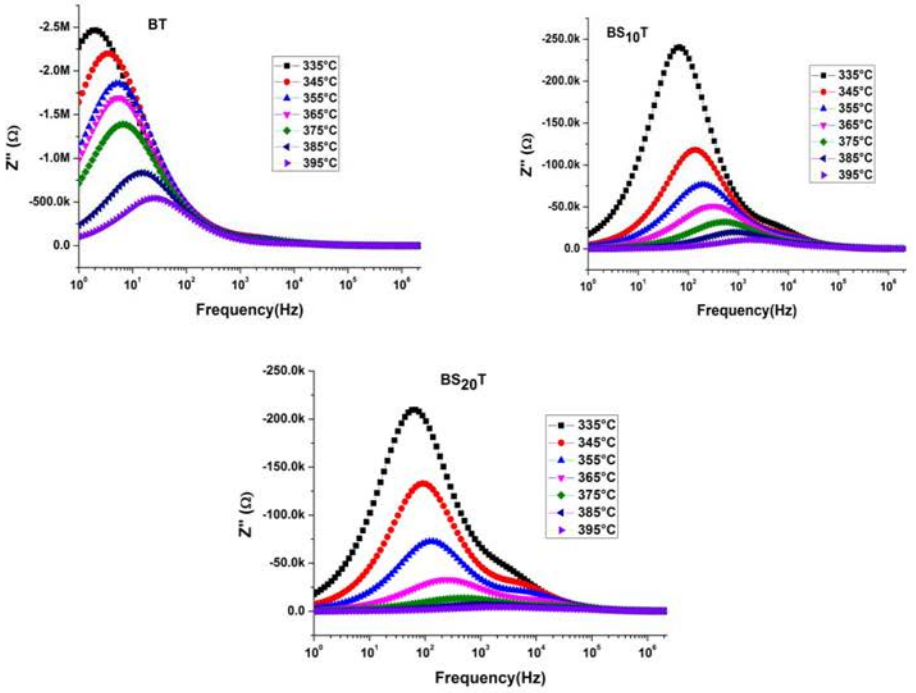

(b)

Fig. 16.a. variation of Z' as a function of the frequency for ceramics $Ba_{1-x}Sr_xTiO_3$.
Fig. 16.b. Variation of Z'' as a function of frequency for $Ba_{1-x}Sr_xTiO_3$ ceramics.

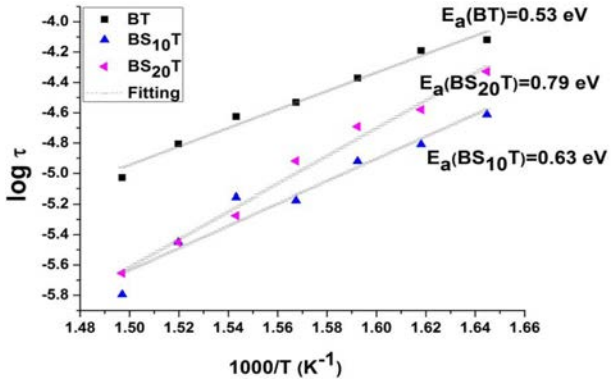

Fig. 17. Variation of the relaxation time as a function of 1000/T.

may be due to the migration of charge carriers over a long distance or to the relaxation bias mechanism over a short distance. In dielectric materials, which are our case, the electrical conductivity is mainly attributed to the jump of polarons in the material.

The electrical conductivity can be determined from the dielectric data with the help of the following relation:

$$\sigma = 2\pi f \varepsilon_0 \varepsilon'' \quad (9)$$

Where f is the frequency (Hz), ε_0 is the permittivity of vacuum ($8.854*10^{-12}$ F/m) and ε'' is the imaginary part

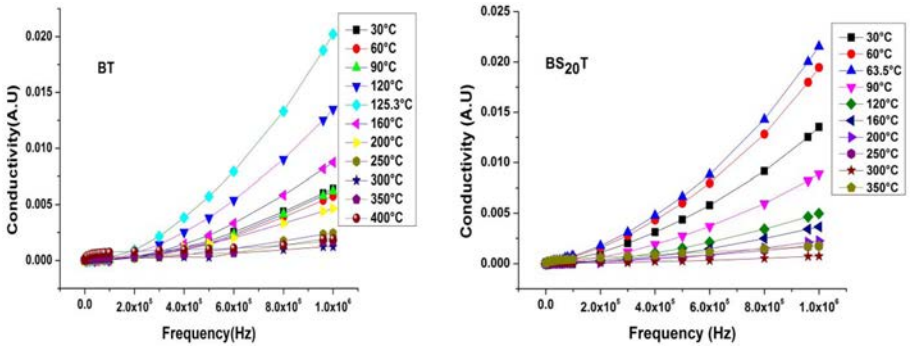

Fig. 18. Variation of conductivity as a function of frequency for $Ba_{1-x}Sr_xTiO_3$ ceramics, with x = 0 and 0.20.

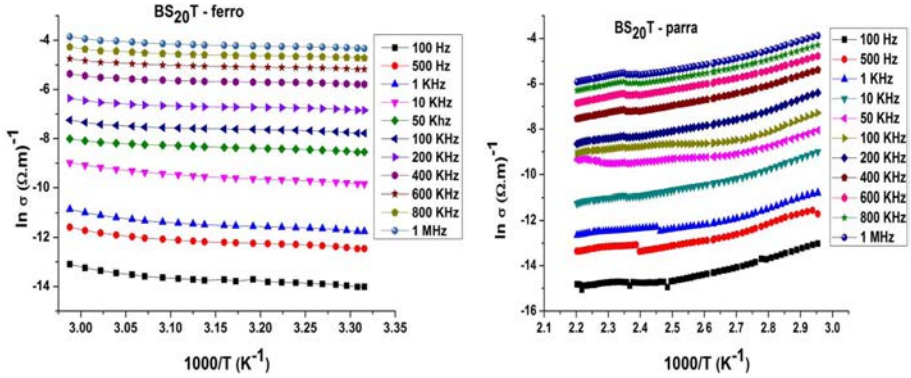

Fig. 19. Variation of the conductivity as a function of 1000/T.

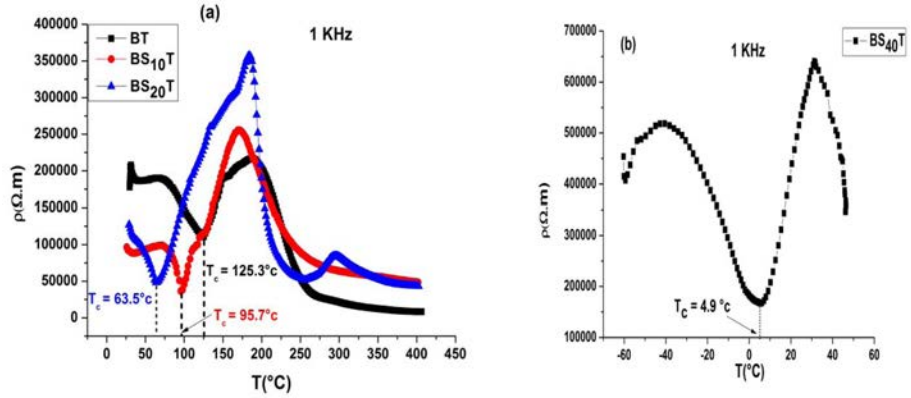

Fig. 20. Thermal variation of resistivity of samples: (a) BT, $BS_{10}T$, $BS_{20}T$ and (b) $BS_{40}T$.

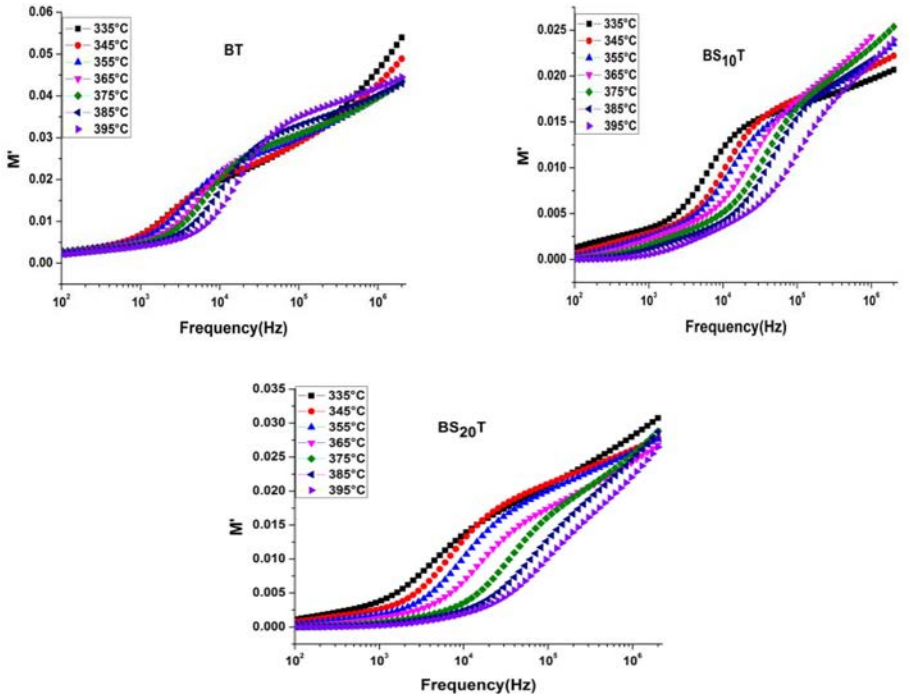

Fig. 21. Variation of M' as a function of frequency for $Ba_{1-x}Sr_xTiO_3$ ceramics.

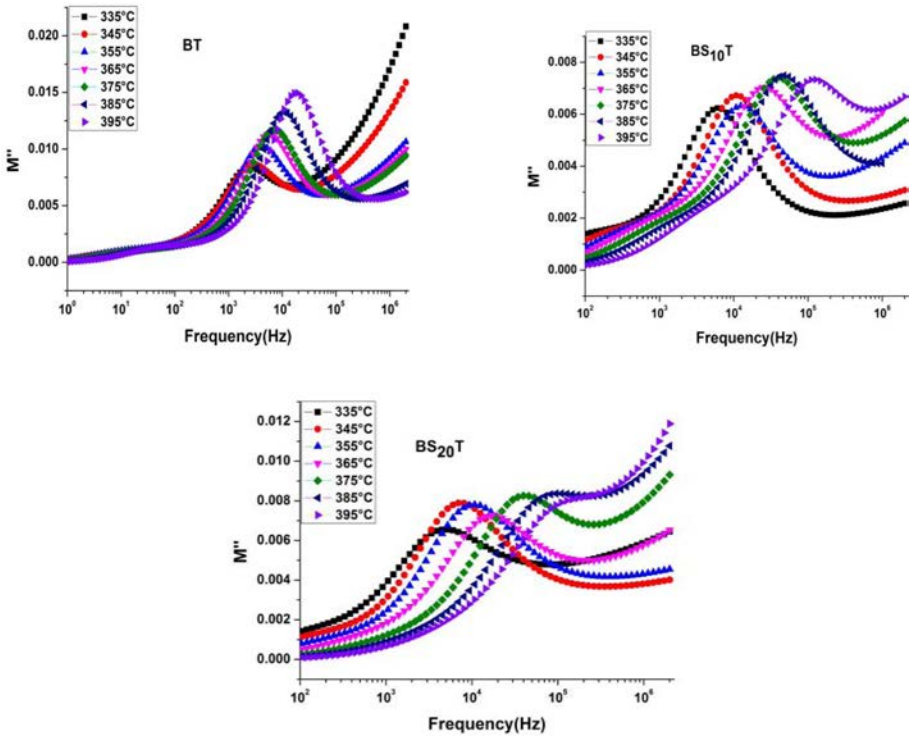

Fig. 22. Variation of M '' as a function of frequency for $Ba_{1-x}Sr_xTiO_3$ ceramics.

of the dielectric permittivity.

Fig. 18 shows, as illustration, the frequency dependence of the conductivity, at different temperatures, for BT and $BS_{20}T$. It is noted that with increasing frequency, σ shows an almost frequency independent behavior followed by a dispersion above a certain frequency (region where σ is sensitive to both frequency and temperature) [42]; the observed increase may be attributed to the relaxation phenomenon. Moreover, for a given frequency, σ increases first with temperature until the ferro-to-paraelectric transition temperature and then decreases.

Fig. 19 displays the variation of σ as a function of

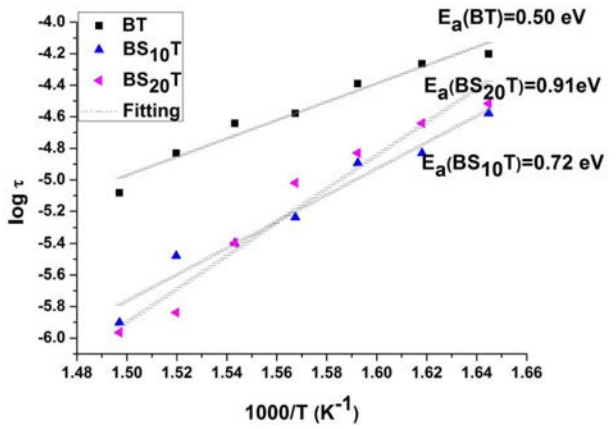

Fig. 23. Variations of relaxation time as functions of 1000/T for BT, $BS_{10}T$ and $BS_{20}T$.

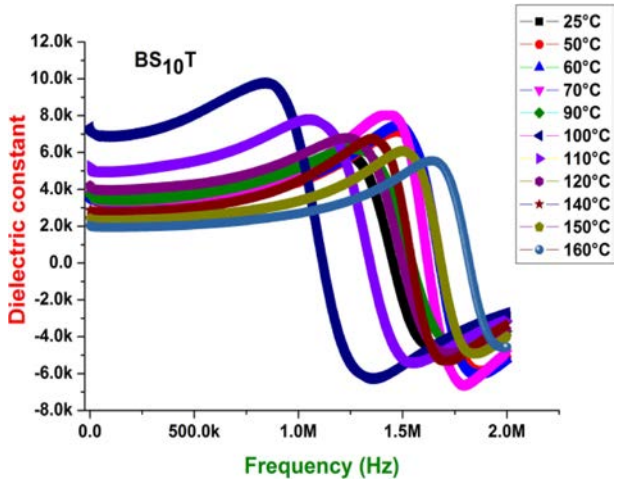

Fig. 24. Variation of dielectric permittivity with frequency for BS10T sintered at 1200 °C.

1000/T, for $BS_{20}T$ below and above the transition temperature.

It is observed that σ first increases (below T_c) with increasing temperature, and then, above T_c, decreases. This behavior, in accordance with that observed on Fig. 18, may be explained as due to the existence of the Positive Temperature Coefficient of Resistivity (PTCR effect).

Indeed, as revealed by the curves corresponding to thermal variations of resistivity (Fig. 20(a and b)), the latter decreases until T_c and then increases. This effect is maximum for the sample with 20% in Sr. A good PTCR material should have a high ratio of the maximum electrical resistivity to the minimum room temperature resistivity and high capability to maintain its high electrical resistivity over the long range of temperature above its Curie point. In doped $BaTiO_3$ ceramics the PTCR jumps by 3 to 7 orders of magnitude. This jump for the $BS_{10}T$ sample is about 3.5 order of magnitude, and may be improved through optimizations and processing and its different related parameters.

Modulus spectra

Analysis and interpretation of the dynamic aspects of electric transport phenomena may be carried out with the help of complex modulus which provides informations about the electrical processes characterized by the smallest capacity of the material, the representation of the electric modulus suppresses the undesirable effects of extrinsic relaxation. Indeed, in the M* formalism, the spatial charge effects and polarization of the electrodes and the grain-boundary conduction process can be suppressed

Table 5. Estimated values of equivalent circuit parameters.

$BS_{10}T$												
T (°C)	Q_1 (pF)	R_1 (kΩ)	n_1	C_1 (nF)	τ_1 (10^{-6} S)	f_{1max} (Hz)	Q_2 (nF)	R_2 (kΩ)	n_2	C_2 (nF)	τ_2 (10^{-4} S)	f_{2max} (Hz)
3 35	885	30.7	0.99	0.7958	27.2	6514	9.880	611	0.85	4.0099	60.4	65
345	923	18.8	0.99	0.8263	17.4	10246	11.500	305	0.84	3.9181	35.1	133
355	1012	13.3	0.99	0.9036	13.5	13243	16.400	212	0.80	3.9823	34.8	188
365	1073	7	0.99	0.9524	7.5	23872	19.600	147	0.77	3.4153	28.8	317
375	1075	5.1	0.99	0.9512	5.5	22808	19.900	91	0.78	3.3530	18.1	522
385	1078	4.8	0.97	0.7398	5.2	44818	18.517	54	0.81	3.6632	9.99	805
395	1395	1.5	0.98	1.0682	2.09	99325	24.027	31	0.77	2.7949	7.45	1837
$BS_{20}T$												
T (°C)	Q_1 (pF)	R_1 (kΩ)	n_1	C_1 (nF)	τ_1 (10^{-6} S)	f_{1max} (Hz)	Q_2 (nF)	R_2 (kΩ)	n_2	C_2 (nF)	τ_2 (10^{-3} S)	f_{2max} (Hz)
3 35	2267	56	0.90	0.8366	127	3397	13.445	556	0.82	4.5898	7.47	62
345	1289	42.7	0.93	0.6161	55.1	6049	13.550	335	0.85	5.2296	4.54	91
355	1533	31.5	0.92	0.6459	48.3	7821	20.360	188	0.83	6.5120	3.83	130
365	1537	15.5	0.94	0.7791	23.8	13179	42.999	98	0.75	6.9452	4.21	234
375	1391	7	0.95	0.7578	9.74	30003	95.871	45.2	0.68	7.4064	4.33	476
385	2807	3.9	0.91	0.9070	10.9	44992	112.77	24.3	0.67	6.1314	2.74	1062
395	2782	1.98	0.93	1.1182	5.51	71884	129.41	15.2	0.65	4.5164	1.97	2318

Table 6. Activation energy values obtained from Fig. 18

	BT	$BS_{10}T$	$BS_{20}T$
E_a (eV)	0.53	0.63	0.79

[43, 44].

The complex electrical modulus (M *) is defined as a function of complex dielectric permittivity (ε *) by the following relation:

$$M^* = \frac{\varepsilon'}{\varepsilon'^2+\varepsilon''^2} + i\frac{\varepsilon''}{\varepsilon'^2+\varepsilon''^2} = M' + iM'' \quad (7)$$

Or M 'and M" are respectively the real and imaginary part of the complex electric modulus M*

Fig. 21 shows the variation of the real part of the electric modulus (M') as a function of frequency, at high temperatures (between 335 °C and 395 °C). Low values of M' are observed in the low frequency region followed by a continuous dispersion with increasing frequency. It is also observed that the obtained curves may be approached by three plateaus (Fig. 21), the first and the third having approximately the same slope. After a first slight increase (first plateau), a quite strong change in the slope is observed (second plateau) within a certain frequency interval, followed by a second change in slope leading to a similar tendency (similar slope) of increase as of the first plateau; a 'break' in the behavior occurs in a certain domain of frequency probably due to the short range mobility of carriers such as ions. Moreover, M' shows a dispersion tending towards $M_{(infini)}$, the asymptotic value of M' at high frequencies.

Fig. 22 shows the frequency dependence of the imaginary part, M'', of the electric modulus at different temperatures. M'' exhibits a maximum which shifts to higher frequencies with increase in temperature. This peak observed in the plot of M'' as a function of frequency corresponds to a relaxation process. The frequency region below this maximum of M'' gives the extent to which charge carriers are mobile on long distances (Jump conduction process). At the frequencies above this maximum the carriers are confined to potential wells and hence are mobile on short distances [45].

Moreover, the widening of the observed asymmetric peak (Fig. 22) may be related to the existence of a distribution of relaxation times.

The frequency ω_{max} (corresponding to M''_{max}) gives the relaxation time τ from the condition $\omega_{max}.\tau = 1$. Taking into account this condition, Fig. 23 displays variation of relaxation time as a function of 1000/T. As for this parameter calculated from Z'' data, the activation energy increases with increasing Sr content, and its corresponding values are quite similar to those obtained from fitting of M'' data to an Arrhenius law (Fig. 23).

Study of the piezoelectric properties of BSxT.

Piezoelectric study has been carried out on the sample $BS_{10}T$.

The piezoelectric coefficients were determined using the resonance-antiresonance frequencies from fig. 24, for each temperature [46, 47].

The planar electromechanical coupling factor Kp was determined with the help of the following relation:

$$K_p^2 = \frac{\eta^2-(1-\alpha^{E^2})}{2(1+\alpha^E)} * \frac{f_a^2-f_r^2}{f_a^2} = 1.255 * \frac{f_a^2-f_r^2}{f_a^2} \quad (10)$$

Young Module E

$$E = \left[\frac{\pi\phi f_r}{\eta}\right]^2 * (1-\alpha^{E^2}) * d(N/m^2) \quad (11)$$

The piezoelectric constant of charge d

$$d^A = K_P{}^A \sqrt{\frac{(1-\alpha^E)\varepsilon_r\varepsilon_0}{2E}} (C/N) \text{ at } 25\ ^\circ\text{C} \quad (12)$$

The voltage constant g

$$g^A = \frac{d^A}{\varepsilon_r\varepsilon_0} (m.V/N) \text{ at } 25\ ^\circ\text{C} \quad (13)$$

Calculation of the piezoelectric charge constant d^B and the voltage constant g^B at high temperatures was done

Table 7. gathers values of the piezoelectric parameters of the sample $BS_{10}T$ heat treated at 1200°C.

	T (°C)	f_r (MHz)	f_a (MHz)	ε_r	K_p	E (10^{12}N.m^{-2})	d^B (10^{-12}C.N^{-1})	g^B (10^{-3}V.m.N^{-1})
$BS_{10}T$ (1200°C)	50	1.477	1.873	7101	0.69	2.78737s	50.44659	0.80264
	60	1.485	1.865	7412	0.68	2.81764	48.31719	0.73657
	70	1.43	1.794	8092	0.68	2.61279	47.93066	0.66925
	90	1.271	1.774	6218	0.78	2.06407	71.07194	1.29142
	100	0.829	1.342	9763	0.88	0.87809	98.02649	1.13448
	110	1.073	1.563	7782	0.81	1.47107	78.43805	1.1389
	120	1.238	1.728	6779	0.78	1.95828	69.88494	1.16477
	140	1.355	1.706	6732	0.68	2.34591	55.80408	0.93668
	150	1.502	1.845	6063	0.65	2.88252	50.70086	0.94484
	160	1.64	1.98	5550	0.63	3.43653	46.82705	0.95335

using the following relations:

$$d^B = d^A \frac{K_P{}^B f_r^A}{K_P{}^A f_r^B} \sqrt{* \frac{\varepsilon_r^A}{\varepsilon_r^B}} \text{ (14) and } g^B = \frac{d^B}{\varepsilon_0 \varepsilon^B{}_r} \quad (15)$$

With:

Φ: Diameter of the sample (m)

α^E: The poisson coefficient (0.31 for ceramics)

η: The root of the Bessel equation (η = 2.05)

d: Density (Kg / m^3)

ε_0: is the permittivity of free space ($8.854*10^{-12}$ F/m)

ε_r: The relative permittivity

f_r: Resonance Frequency(Hz)

f_a: Anti-resonance frequency(Hz)

The planar electromechanical coupling factor Kp, representes the ability of a ceramic to transform electrical energy into mechanical energy. Values given in Table 7 show that this factor increases first with increasing temperature and reaches its maximum value around the ferro-to-paraelectric transition (96°C) and then decreases. The increase in Kp may be due to the fact that during the polarization of the material the degree of alignment of the domains increases (Kp increases) and becomes higher in the coexisting region of the cubic and tetragonal phases. The decrease of Kp may be due to the fact that the increase in temperature favors the mobility of the ions, which causes a disorder of the dipole moments which are randomly oriented.

In the same time, the young's modulus shows a decrease with temperature until its minimum value in the vicinity of T_C. Beyond this value there is an increase of this factor. The decrease of this factor as a function of temperature may be due to the rupture of some bonds in the material, and thus the attraction forces prevent the vibration of the dipoles [48].

The piezoelectric coefficient of charge, d^B, follows the same variations as of Kp (Table 7); this coefficient also reaches its maximum value around T_c and then decreases. This decrease may be due to thermal agitations that are responsible for the disorder in the material.

It is clear from then that optimum values of dielectric permittivity and piezoelectric parameters are observed around the ferro-to-paraelectric transition temperature.

Conclusions

Structural, dielectric and piezoelectric properties of sol gel processed $Ba_{1-x}Sr_xTiO_3$ (x = 0.00; 0.10; 0.20; 0.30 and 0.40) nanopowders were investigated. Pure perovskite structure was obtained under heating at 900 ºC during 3h. Sr doping transforms the structure of the pure sample ($BaTiO_3$) from quadratic to pseudocubic. The average crystallite size was about 30 nm. Dielectric studies reveal that Sr doping lowers the temperature of the ferro-to-paraelectric _transition accompanied with relaxation and diffusness for x > 0.10. Modified Uchino's law was used to describe the thermal paraelectric behavior of the permittivity. Investigation of the conduction phenomenon in these samples reveals the presence of the PTCR effect, which was prominent for x = 0.20. Optimum values of the piezoelectric parameters were obtained around the Curie temperature.

References

1. L.H. Parker, A.F. Tasch, IEEE Circuits Devices Mag. 6 (1990) 17-26.
2. T. Kawaguchi, H. Adachi, K. Setsune, O.Y. Amazaki, K. Wasa, Appl. Opt. 23 (1984) 2187-2191.
3. K.K. Deb, Ferroelectrics 82 (1998) 45-53.
4. L.A. Thomas, Ferroelectrics 3 (1972) 231-238.
5. D.Y. Lu, Y. Yue, X.Y. Sun, J. Alloys Compd. 586 (2014) 136-141.
6. S.K. Rout, J. Bera, in: A.P. Tandon (Ed.), Allied Publishers Pvt. Ltd., New Delhi. (2004) 3-7.
7. C. Fu, C. Yang, H. Chen, Y. Wang, L. Hu, Mater. Sci. Eng. B., 119 (2005) 185-188.
8. O.P. Thakur, C. Prakash, D.K. Agarwal, Mater. Sci. Eng., B. 96 (2002) 221-225.
9. R.M. Mahani, I.K. Battisha, M. Alyb, A.B. AbouHamad, J. Alloys Compd. 508 (2010) 354-358.
10. M. Veith, S.MTHUR, N. LECERF, V. Huch, T. Decker. J. Sol-Gel Sci. technol. 15 (2000) 145-158.
11. L. Wei, X. Zhijun, C. Ruiqing, F. Peng, H. Jigong, J. Alloys Compd. 482 (2009) 137-140.
12. D. Fengtao, C. Bin, C. Hualei, N. Ruiyuan, C. Zhuguo, Mater. Res. Bull. 44 (2009) 1930-1934.
13. P. M.M. Vijatović, J.D. Bobić, T. Ramoška, J. Banys, B.D. Stojanović , Mater. charact. 62 (2011) 1000-1006.
14. A. Elbasset, F. Abdi, T. Lamcharfi, S. Sayouri, M. Aillerie. IREPHY. 7[3] (2013) 287-293.
15. B.D. Cullity, Elements of X-ray diffraction, Addison-Wesley publishing Company Inc., 1956.
16. E. V. Ramana, F. Figueiras, A. Mahajan, D. M. Tobaldi, B.F.O. Costa, M.P.F. Graça and M. A. Valente. J. Mater. Chem. C[4] (2016) 1066-1079.
17. J.T. Last, Phys. Rev., 105 (1957) 1740-50.
18. N.W. Alock, V.M. Tracy, and T.C. Waddington, J. Chem. Soc., Dalton Trans., (1976) 2243-46.
19. E. Sanchez, T. Lopez, R. Gomea, A. Morales and O. Novaro, J. Solid State Chem., 122 (1996) 309-14.
20. U.D. Venkateswaran, V.M. Naik, R. Naik, Phys. Rev. B. 58 (1998) 14256-60.
21. P. Hermet, M. Veithen, P. Ghosez, J. Phys.: Condens. Matter. 21 (2009) 215901.
22. Y. Xu, Ferroelectric Materials and Their Applications. North-Holland: Amsterdam, 1991.
23. A. Helmi, H. Khemakhem, G. V`elu, J.C. Carru, R.V.D. M¨uhll, Solid State Sci. 6 (2004) 1347-1351.
24. B. S. Kang, S. K. Shoi and C. H. Park, J. Appl. Phys. 94[3] (2003)1904-1911.
25. I. Adelina, B. Daniela, V. Massimo, E.C. Cristina, M. Liliana, V. Eugeniu, D. Nicolae, C. Dorel, J. Eur. Ceram. Soc. 27 (2007) 3655-3658.
26. K. Manoj, G. Ashish, K. Ravi, M.C. Bhatnagar, Physica B 403 (2008)1819-1823.
27. T. Chanyaphak, T. Sarawut, Ceram. Int. 41(2015) S95-S99.
28. A. Ianculescu, I. Pintilie, C.A. Vasilescu, M. Botea, A. luga, A. Melinescu, N. Dragan, L. Pintilie, Ceram. Int. 42

(2016) 10338-10348.
29. L. Wei, X. Zhijun, C. Ruiqing, F. Peng, H. Jigong, J. Alloys Compd. 499 (2010) 255-258
30. L. Nedelcu, A. Ioachim, M. Toacsan, M.G. Banciu, I. Pasuk, C. Berbecaru, H.V. Alexandru, Thin Solid Films 519 (2011) 5811-5815.
31. S. Lahiry, A. Mansingh, Thin Solid Films 516 (2008) 1656-1662.
32. M.E. Lines, A.M. Glass, Principles and Applications of Ferroelectrics and Related Materials, Oxford University Press, Oxford, 1977.
33. J. Ravez, A. Simon, CR Acad. Sci. 325 (1997) 481.
34. N.S. Echatoui, T. Lamcharfi, S. Sayouri, L. Hajji, A. Alimoussa, Phys. Chem. News, 26 (2005) 40-46.
35. L.E. Cross, Ferroelectrics 151 (1994) 305.
36. A.R. Muhammad, N.R. Muhammad, K.V. Sarvanan, Ceram. Int. 41 (2015) 11436-11444.
37. D. Chen, R.Ran, K. Zhang, J. Wang, Z. Shao, J. Power Sources 188 (2009) 96.
38. K. Prabakar, S.A.K. Narayandass, D. Mangalaraj, Cryst. Res. Technol. 37 (2002) 1094.
39. A.A. Saif, P. Poopalan, Physica B, 406 (2011) 1283-1288.
40. S. Sen, R.N.P. Choudhary, Mater.Chem.Phys. 87[2-3] (2004) 256-263.
41. A.K. Jonscher,The universal dielectric response, Nature 267[5613] (1977) 673-679.
42. S.R. Elliot, Philos. Mag. 36 (1977) 1291.
43. R.M. Neagu, E. Neagu, J. Appl. Phys. 88[11] (2000) 6669.
44. S.A. Saafan, S.A. Seoud, R.E. El Shafer, Physica B 365 (2005) 27.
45. C.R.K. Mohan, R. Dey, S. P. Patel, R.K. Pandey, M.P. Sharma, P.K. Bajpai, Nucl. Instrum. Methods Phys. Res. B. 372 (2016) 50-57.
46. B. Jaffe, S. Roth, S. Marzullo, J. Res. Natl. Bur. Stand. 55 (1955) 239-254.
47. W. P. Mason, B. Jaffe, Proceedings of the IRE, 42[6] (1954) 921-930.
48. A. Boutarfaia, S.E. Bouaoud, Ceram. Int., 22[4] (1996) 281-286.